Spectral-interference microscopy for characterization of functional plasmonic elements

Christian Rewitz,[1] Thomas Keitzl,[1] Philip Tuchscherer,[1] Sebastian Goetz,[1] Peter Geisler,[2] Gary Razinskas,[2] Bert Hecht,[2,3,4] and Tobias Brixner[1,3,*]

[1]*Institut für Physikalische und Theoretische Chemie, Universität Würzburg, Am Hubland, 97074 Würzburg, Germany*

[2]*Nano-Optics and Biophotonics Group, Experimentelle Physik 5, Universität Würzburg, Am Hubland, 97074 Würzburg, Germany*

[3]*Röntgen Center for Complex Material Systems (RCCM), Am Hubland, 97074 Würzburg, Germany*

[4]*hecht@physik.uni-wuerzburg.de*

[*]*brixner@phys-chemie.uni-wuerzburg.de*

Abstract: Plasmonic modes supported by noble-metal nanostructures offer strong subwavelength electric-field confinement and promise the realization of nanometer-scale integrated optical circuits with well-defined functionality. In order to measure the spectral and spatial response functions of such plasmonic elements, we combine a confocal microscope setup with spectral interferometry detection. The setup, data acquisition, and data evaluation are discussed in detail by means of exemplary experiments involving propagating plasmons transmitted through silver nanowires. By considering and experimentally calibrating any setup-inherent signal delay with an accuracy of 1 fs, we are able to extract correct timing information of propagating plasmons. The method can be applied, e.g., to determine the dispersion and group velocity of propagating plasmons in nanostructures, and can be extended towards the investigation of nonlinear phenomena.

OCIS codes: (120.4820) Optical systems; (130.2790) Guided waves; (180.3170) Interference microscopy; (180.5810) Scanning microscopy; (250.5403) Plasmonics; (300.6310) Spectroscopy, heterodyne; (320.7085) Ultrafast information processing; (320.7120) Ultrafast phenomena.

References and links

1. R. Zia, J. A. Schuller, A. Chandran, and M. L. Brongersma, "Plasmonics: the next chip-scale technology," Mater. Today **9**, 20–27 (2006).
2. E. Ozbay, "Plasmonics: Merging photonics and electronics at nanoscale dimensions," Science **311**, 189–193 (2006).
3. D. K. Gramotnev and S. I. Bozhevolnyi, "Plasmonics beyond the diffraction limit," Nat. Photonics **4**, 83–91 (2010).
4. P. Mühlschlegel, H. Eisler, O. J. F. Martin, B. Hecht, and D. W. Pohl, "Resonant optical antennas," Science **308**, 1607–1609 (2005).
5. J.-S. Huang, T. Feichtner, P. Biagioni, and B. Hecht, "Impedance matching and emission properties of nanoantennas in an optical nanocircuit," Nano Lett. **9**, 1897–1902 (2009).
6. J. Wen, S. Romanov, and U. Peschel, "Excitation of plasmonic gap waveguides by nanoantennas," Opt. Express **17**, 5925–5932 (2009).

#166965 - $15.00 USD
Received 18 Apr 2012; accepted 20 May 2012; published 15 Jun 2012

7. S. I. Bozhevolnyi, V. S. Volkov, E. Devaux, J. Laluet, and T. W. Ebbesen, "Channel plasmon subwavelength waveguide components including interferometers and ring resonators," Nature **440**, 508–511 (2006).
8. A. A. Reiserer, J. Huang, B. Hecht, and T. Brixner, "Subwavelength broadband splitters and switches for femtosecond plasmonic signals," Opt. Express **18**, 11810–11820 (2010).
9. H. Wei, Z. Li, X. Tian, Z. Wang, F. Cong, N. Liu, S. Zhang, P. Nordlander, N. J. Halas, and H. Xu, "Quantum Dot-Based local field imaging reveals Plasmon-Based interferometric logic in silver nanowire networks," Nano Lett. **11**, 471–475 (2011).
10. H. Wei, Z. Wang, X. Tian, M. Kall, and H. Xu, "Cascaded logic gates in nanophotonic plasmon networks," Nat. Commun. **2**, 387 (2011).
11. V. V. Temnov, U. Woggon, J. Dintinger, E. Devaux, and T. W. Ebbesen, "Surface plasmon interferometry: measuring group velocity of surface plasmons," Opt. Lett. **32**, 1235–1237 (2007).
12. H. Ditlbacher, A. Hohenau, D. Wagner, U. Kreibig, M. Rogers, F. Hofer, F. R. Aussenegg, and J. R. Krenn, "Silver nanowires as surface plasmon resonators," Phys. Rev. Lett. **95**, 257403 (2005).
13. M. Allione, V. V. Temnov, Y. Fedutik, U. Woggon, and M. V. Artemyev, "Surface plasmon mediated interference phenomena in Low-Q silver nanowire cavities," Nano Lett. **8**, 31–35 (2008).
14. L. Lepetit, G. Chériaux, and M. Joffre, "Linear techniques of phase measurement by femtosecond spectral interferometry for applications in spectroscopy," J. Opt. Soc. Am. B **12**, 2467–2474 (1995).
15. C. Ropers, G. Stibenz, G. Steinmeyer, R. Müller, D. Park, K. Lee, J. Kihm, J. Kim, Q. Park, D. Kim, and C. Lienau, "Ultrafast dynamics of surface plasmon polaritons in plasmonic metamaterials," Appl. Phys. B **84**, 183–189 (2006).
16. R. Rokitski, K. A. Tetz, and Y. Fainman, "Propagation of femtosecond surface plasmon polariton pulses on the surface of a nanostructured metallic film: Space-Time complex amplitude characterization," Phys. Rev. Lett. **95**, 177401 (2005).
17. M. L. M. Balistreri, H. Gersen, J. P. Korterik, L. Kuipers, and N. F. van Hulst, "Tracking femtosecond laser pulses in space and time," Science **294**, 1080–1082 (2001).
18. M. Sandtke, R. J. P. Engelen, H. Schoenmaker, I. Attema, H. Dekker, I. Cerjak, J. P. Korterik, B. Segerink, and L. Kuipers, "Novel instrument for surface plasmon polariton tracking in space and time," Rev. Sci. Instrum. **79**, 013704 (2008).
19. A. W. Sanders, D. A. Routenberg, B. J. Wiley, Y. Xia, E. R. Dufresne, and M. A. Reed, "Observation of plasmon propagation, redirection, and Fan-Out in silver nanowires," Nano Lett. **6**, 1822–1826 (2006).
20. Y. Fang, Z. Li, Y. Huang, S. Zhang, P. Nordlander, N. J. Halas, and H. Xu, "Branched silver nanowires as controllable plasmon routers," Nano Lett. **10**, 1950–1954 (2010).
21. R. Yan, P. Pausauskie, J. Huang, and P. Yang, "Direct photonic–plasmonic coupling and routing in single nanowires," Proc. Natl. Acad. Sci. USA **106**, 21045–21050 (2009).
22. Z. Li, K. Bao, Y. Fang, Y. Huang, P. Nordlander, and H. Xu, "Correlation between incident and emission polarization in nanowire surface plasmon waveguides," Nano Lett. **10**, 1831–1835 (2010).
23. L. Novotny and B. Hecht, *Principles of Nano-Optics* (Cambridge University Press, 2006).
24. C. Dorrer and M. Joffre, "Characterization of the spectral phase of ultrashort light pulses," C. R. Acad. Sci., Ser. IV: Phys. **2**, 1415–1426 (2001).
25. Z. Bor, "Distortion of femtosecond laser pulses in lenses and lens systems," J. Mod. Opt. **35**, 1907–1918 (1988).
26. C. Radzewicz, M. la Grone, and J. Krasinski, "Interferometric measurement of femtosecond pulse distortion by lenses," Opt. Commun. **126**, 185–190 (1996).
27. C. Rewitz, T. Keitzl, P. Tuchscherer, J. Huang, P. Geisler, G. Razinskas, B. Hecht, and T. Brixner, "Ultrafast plasmon propagation in nanowires characterized by Far-Field spectral interferometry," Nano Lett. **12**, 45–49 (2012).
28. C. Dorrer, N. Belabas, J. Likforman, and M. Joffre, "Spectral resolution and sampling issues in Fourier-transform spectral interferometry," J. Opt. Soc. Am. B **17**, 1795–1802 (2000).
29. M. I. Stockman, S. V. Faleev, and D. J. Bergman, "Coherent control of femtosecond energy localization in nanosystems," Phys. Rev. Lett. **88**, 067402 (2002).
30. J.-S. Huang, D. V. Voronine, P. Tuchscherer, T. Brixner, and B. Hecht, "Deterministic spatiotemporal control of optical fields in nanoantennas and plasmonic circuits," Phys. Rev. B **79**, 195441 (2009).
31. P. Tuchscherer, C. Rewitz, D. V. Voronine, F. J. G. de Abajo, W. Pfeiffer, and T. Brixner, "Analytic coherent control of plasmon propagation in nanostructures," Opt. Express **17**, 14235–14259 (2009).
32. M. Aeschlimann, M. Bauer, D. Bayer, T. Brixner, S. Cunovic, F. Dimler, A. Fischer, W. Pfeiffer, M. Rohmer, C. Schneider, F. Steeb, C. Strüber, and D. V. Voronine, "Spatiotemporal control of nanooptical excitations," Proc. Natl. Acad. Sci. USA **107**, 5329–5333 (2010).
33. L. Cao, R. A. Nome, J. M. Montgomery, S. K. Gray, and N. F. Scherer, "Controlling plasmonic wave packets in silver nanowires," Nano Lett. **10**, 3389–3394 (2010).
34. M.-T. Cheng, Y.-Q. Luo, P.-Z. Wang, and G.-X. Zhao, "Coherent controlling plasmon transport properties in metal nanowire coupled to quantum dot," Appl. Phys. Lett. **97**, 191903 (2010).
35. S. Mukamel, *Principles of Nonlinear Optical Spectroscopy* (Oxford University Press, 1999).

#166965 - $15.00 USD Received 18 Apr 2012; accepted 20 May 2012; published 15 Jun 2012

1. Introduction

Integrated plasmonic circuitry is discussed as a candidate for the next optical data processing chip-scale technology since it offers subwavelength confinement of guided light fields in combination with the possibility to devise well-defined functional elements [1–3]. The building blocks of integrated circuits include optical antennas for an efficient interconversion of far-field and near-field modes [4–6] as well as plasmonic waveguides with particular routing functions such as splitting [7, 8], filtering [7] and switching [8–10].

So far, much work related to the characterization of transport properties of suitable nanostructures relies on simulations and local near-field measurements, thus providing some insight into characteristic optical properties. However, to accurately assess the overall function and performance of plasmonic elements, it is important to investigate relevant parameters such as the speed of plasmon propagation in a work environment. In Fig. 1 such a setting is sketched. It includes a far-field light source that locally excites guided plasmons, a functional plasmonic element, which processes the guided waves, and an outcoupling region where guided plasmons are converted back into far-field propagating photons.

The spectral analysis of white light transmitted through plasmonic metal films with slit–groove pairs yielding the group velocity of two-dimensional surface plasmons [11] has been an approach to this setting without using high spatial resolution. Furthermore, interference of plasmons in nanowires acting as resonators has been detected at the distal and the input end of these nanowires to determine plasmon losses and group velocities [12, 13]. However, both methods rely on self-interference of plasmons and, hence, are limited, e.g., with respect to the geometry of the nanostructure.

In contrast, the heterodyne technique of spectral interferometry [14] employs a delayed reference pulse together with spectrally resolved detection for full characterization (amplitude and phase) of electric fields, e.g., transmitted through a periodic nanoslit/-hole array using weakly focused fields [15]. In a related heterodyne technique the interference is detected without spectral resolution and the delay time between signal and reference pulse has to be scanned. This technique has been used previously to characterize propagation of plasmon pulses on the surface of a nanostructured metallic film [16]. A combination of this technique with near-field microscopy has been implemented to characterize the propagation of pulsed evanescent fields in photonic [17] and plasmonic waveguides [18].

In this work, we discuss a technique where a confocal microscope is combined with spectral interferometry. The excitation and detection position can be chosen independently, thus enabling optical excitation of a certain structure at one spot while monitoring its emission at another spot. Hence, we can measure complete spectral response functions with spatial resolution. The technique enables us to, e.g., characterize group velocities of propagating plasmons in optically integrated nanostructures (Fig. 1). For the determination of these group velocities time delays due to geometrical path differences within the setup have to be taken into account, as we will show in Section 4.

2. Experimental setup

For the experimental implementation of the scenario outlined in Fig. 1 we use a confocal microscope that has the ability of selectively detecting particular emission spots independent of the excitation position. Heterodyne detection is then realized with a reference beam. The experimental setup is shown in Fig. 2. A polarizer ensures that the excitation polarization of the femtosecond laser pulses [peak wavelength $\lambda_0 = 800$ nm, spectral full width at half-maximum (FWHM) = 46 nm] is linearly polarized. Since the analyzer selects the respective orthogonal polarization component of the emission signal, a crossed-polarizer scheme can be used in order to suppress reflected light. The first beam splitter BS_1 reflects 8% of the incoming (*s* polar-

#166965 - $15.00 USD Received 18 Apr 2012; accepted 20 May 2012; published 15 Jun 2012

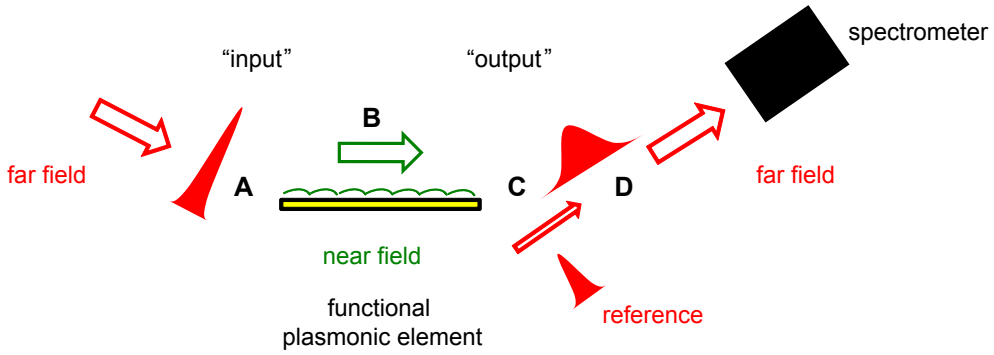

Fig. 1. Scenario of optically integrated plasmonic circuits and response function characterization. A pulsed far-field light source excites propagating plasmons (A) that are processed by functional plasmonic elements (B). After propagation the pulses are converted back into a far-field detectable signals (C) and full characterization (amplitude and phase) is facilitated via spectral interferometry [14] (D).

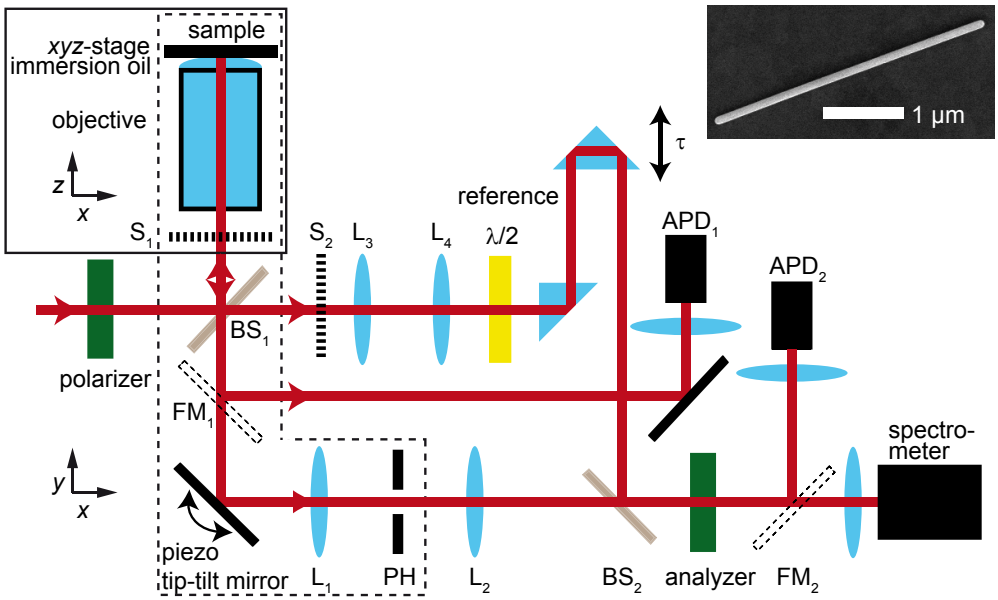

Fig. 2. Scheme of the setup. BS = beam splitter, S = shutter, L = lens, PH = pinhole, FM = flip mirror, APD = avalanche photodiode. The linearly polarized excitation beam is split into a part for excitation and a reference. Signals from the sample plane are redirected by a piezo tip-tilt mirror to pass the pinhole (PH). The reference beam is dispersion compensated by traversing two prisms before being recombined with the signal for spectrally resolved heterodyne detection. The inset shows a scanning electron microscope (SEM) image of a representative silver nanowire with a length of 3.5 μm and a diameter of 90 nm.

#166965 - $15.00 USD
Received 18 Apr 2012; accepted 20 May 2012; published 15 Jun 2012

ized) light towards an immersion-oil objective (Nikon Plan Apo, 100×/1.40) in order to excite nanostructures in the sample plane. The beam diameter is chosen to overfill the back aperture of the objective. An *xyz*-piezo stage (P-517.3CL, PI, Germany) moves the sample relative to the excitation beam position and adjusts the focus. The same objective is also used to collect light emitted from arbitrary positions of the sample plane within its field of view. Most of the collected signal is transmitted through BS_1 ($T_p = 99\%$ and $T_s = 92\%$) and is redirected via a piezo tip-tilt mirror (S-334.2SL, PI, Germany) towards a Keplerian telescope (L_1: $f = 200$ mm and L_2: $f = 50$ mm) with a pinhole (PH; $d = 30$ μm) at the common focal plane. This combination facilitates selection of particular (diffraction-limit sized) spots from the field of view independent of the excitation position. Via a flippable mirror (FM_1) the signal can also be directed to an avalanche photo diode (APD_1, Perkin Elmer, SPCM-CD 2801) without passing the pinhole and the analyzer, i.e., the emission from the sample plane then is detected without extra spatial or polarization selection.

The part of the excitation beam transmitted by BS_1 is used as reference. It also passes a Keplerian telescope (L_3: $f = 220$ mm and L_4: $f = 50$ mm) in order to match the signal-beam diameter. A $\lambda/2$-plate in combination with the analyzer acts as a variable attenuator for the reference beam intensity. The reference beam then traverses two NBK-7 prisms (in total-internal-reflection mode) in order to introduce approximately the same second-order dispersion as caused by the microscope objective. This improves the signal–to–noise ratio of the amplitude and phase reconstruction process, which is described later.

Signal and reference beams are recombined at the second beam splitter (BS_2; equivalent to BS_1), which exhibits high transmission for the signal beam. The second flippable mirror (FM_2) allows switching between another avalanche photo diode (APD_2, Perkin Elmer, SPCM-AQR-13) and a spectrometer [spectrograph (Princeton Instruments, Acton SpectraPro 2500i) and charge-coupled device (e2v, CCD42-10 in Princeton Instruments, Acton Pixis2kB)] as detector. APD_1 is used to generate images when the *xyz*-piezo stage is scanned [cf. Fig. 3(a), "excitation scan"], whereas APD_2 is used as detector when the piezo tip-tilt mirror is scanned [e.g., Figs. 3(b) and 3(c), "emission scans"]. The spectrometer is used to record spectral interferograms at specific positions within these "emission scans" [see Figs. 4(a) and 4(b)]. Signal and reference path lengths are chosen to be equal. One of the prisms is mounted on a translation stage, which makes it possible to adjust the time delay τ between signal and reference pulse.

Here, we demonstrate the capabilities of the setup using chemically grown silver nanowires [PlasmaChem GmbH, Berlin, Germany; see inset of Fig. 2 for a representative scanning electron microscope (SEM) image]. Silver nanowires can be considered as building blocks of future plasmonic nanocircuits and have been studied extensively in this context [9, 12, 19–21]. However, other nanostructures, which support propagating modes, can also be characterized using this method. The nanowires have been deposited on indium tin oxide (ITO)-covered microscope cover slips by drop casting. After evaporation of the solvent (H_2O) the nanowires were embedded in index-matching oil (Type B, Cargille-Sacher Laboratories Inc., NJ, USA).

3. Data acquisition and data evaluation

In order to perform an "excitation scan" we raster scan the sample in the *x*–*y* plane and record the intensity of the reflected signal using APD_1. As a result we get scan images as shown in Fig. 3(a), in which the silver nanowires appear as bright elongated structures due to the increased reflection of light in its immediate vicinity. In these images the excitation pulse polarization is linearly polarized along the *y* axis. The transmission axis of the analyzer is oriented along the *x* axis for realization of a crossed-polarizer scheme in "emission scans". In order to optimize the efficiency for both excitation and emission, we orient the sample such that the nanowire to be characterized has its long axis roughly along the diagonal of our "excitation scan" images.

#166965 - $15.00 USD Received 18 Apr 2012; accepted 20 May 2012; published 15 Jun 2012

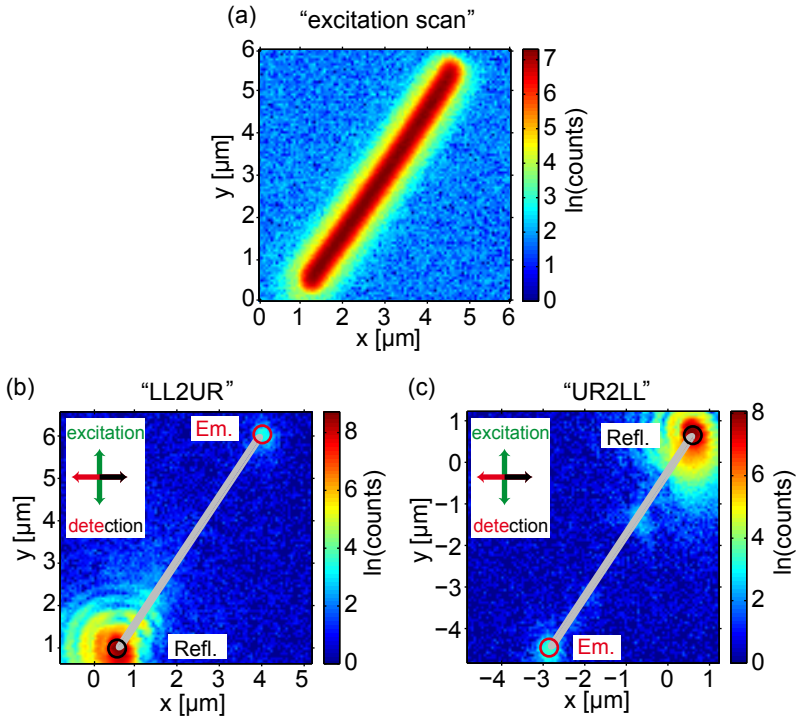

Fig. 3. Example images of plasmon propagation experiments. (a) An “excitation scan” that is used to locate a nanowire is shown. (b) An “emission scan” that is recorded by scanning the piezo tip-tilt mirror is depicted. The reflection of the excitation spot at the lower end of the nanowire (“Refl.”, black circle) and the emission at the upper end of the nanowire (“Em.”, red circle) are visible. Both signals can be completely characterized via spectral interferometry (SI), see Fig. 4. The gray nanowire is sketched for convenience. Since the plasmon propagates from the lower left (LL) to the upper right (UR), we term this measurement “LL2UR-propagation”. (c) The analog experiment for a “UR2LL-propagation” is shown. The insets in (b) and (c) show the excitation and detection polarizations. The axes of (b) and (c) are labeled with respect to the center of the position-dependent pulse arrival time (PD-PAT), which is explained in the corresponding section. Here, the labeling shows that the excitation position (“Refl.”) is the same in measurements (b) and (c) and the nanowire is shifted with respect to this position, as explained in the text.

#166965 - $15.00 USD
Received 18 Apr 2012; accepted 20 May 2012; published 15 Jun 2012

For “emission scans”, this results in a ca. 45° and -45° angle for excitation and detection polarization with respect to the nanowire’s long axis, respectively. Since optimal excitation of plasmons in silver nanowires is typically obtained for a polarization parallel to the nanowire [22], this allows for efficient suppression of reflected light in “emission scans” without severe loss of signal strength.

With the nanowire in the described orientation, there are two options for a plasmon propagation experiment: Either the lower left end of the nanowire is excited and plasmons propagate towards the upper right end (“LL2UR”), where they can be converted back into far-field detectable signals, or the plasmons can be launched at the upper right end and the emission can be detected at the lower left end (“UR2LL”). In either case the respective input end of the nanowire is placed at the position of the excitation focus. With this excitation position fixed, we then use the piezo tip-tilt mirror in the detection path (“emission scan”) to obtain a spatially resolved map of the sample emission as shown in, e.g., Fig. 3(b) (“LL2UR”). In such a map, the direct reflection is readily visible at the excitation position [“Refl.”, black circle in the lower left part of Fig. 3(b)]. The radiative decay of plasmons at the output end can also be observed as a bright spot, which is well separated from the reflection spot for sufficiently long nanowires. This emission can be seen in the upper right part of Fig. 3(b) (“Em.”, red circle). The fact that the directly reflected spot is visible at all in the crossed-polarizer scheme is due to high-numerical-aperture depolarization effects [23] and is exploited to obtain the reference starting time of the plasmon pulse as indicated in Fig. 4(g). The emission intensity can be optimized by fine positioning the nanowire end with respect to the excitation position. Figure 3(c) shows the same experiment for the reverse plasmon propagation direction (“UR2LL”).

Spectral interferometry detection is performed by overlapping the reflected and the emitted pulse after propagation [the signals in the black and red circles of Figs. 3(b) and 3(c), respectively] individually with the reference pulse. Both positions are measured subsequently and the heterodyne signal is recorded with the spectrometer. Even though the amplifying heterodyne detection technique is used, higher excitation intensities than for the avalanche photo diodes are usually required, since the signal is dispersed over many CCD pixels and the used grating is blazed at 500 nm. The respective spectral interferograms corresponding to the experiment shown in Fig. 3(b) are depicted in Fig. 4(a) (reflection, black) and Fig. 4(b) (emission, red). As can be inferred from the modulation of the red line over the complete spectrum, all spectral components of the laser pulse are transmitted through the nanowire.

Amplitude and phase retrieval in spectral interferometry can be achieved by means of a Fourier-transform scheme [14, 24]. For this purpose, the separately measured reference intensity $I_{\mathrm{ref}}(\omega)$ is subtracted from the spectral interferograms and then a first fast Fourier transform is applied. Measurement of the reference intensity $I_{\mathrm{ref}}(\omega)$ is facilitated with computer controlled shutters (by closing shutter S_1 in Fig. 2). Because of the dispersion compensation in the reference beam this first fast Fourier transform yields narrow peaks for the oscillatory part [cf. shaded areas in Figs. 4(c) and 4(d)] and, therefore, enables us to use a relatively short delay time between signal and reference pulse ($\tau \approx 600$ fs), which is well below the Nyquist limit of the detector. The oscillatory parts are then isolated with Fourier windows [shaded areas in Figs. 4(c) and 4(d)] and inversely fast Fourier transformed. This yields complex-valued numbers $S_i(\omega)$, with $i = \mathrm{Refl.}$ and $i = \mathrm{Em.}$, from which the spectral signal intensities $I_i(\omega) = |S_i(\omega)|^2/I_{\mathrm{ref}}(\omega)$ (which can also be measured separately by closing shutter S_2 in Fig. 2) and the difference phases with respect to the reference pulse phase $\varphi_{\mathrm{diff},i}(\omega) = \varphi_i(\omega) - \varphi_{\mathrm{ref}}(\omega) = -\arg S_i(\omega)$ of both signals are calculated as can be seen in Fig. 4(e) and Fig. 4(f). The spectral-phase response function of the plasmonic element can then be calculated by subtracting the retrieved phase of the reflected pulse from that of the emitted pulse, thereby eliminating the reference pulse phase: $\varphi_{\mathrm{response}}(\omega) = \varphi_{\mathrm{diff,Em.}}(\omega) - \varphi_{\mathrm{diff,Refl.}}(\omega)$. As can be deduced from Figs. 4(e) and

#166965 - $15.00 USD Received 18 Apr 2012; accepted 20 May 2012; published 15 Jun 2012

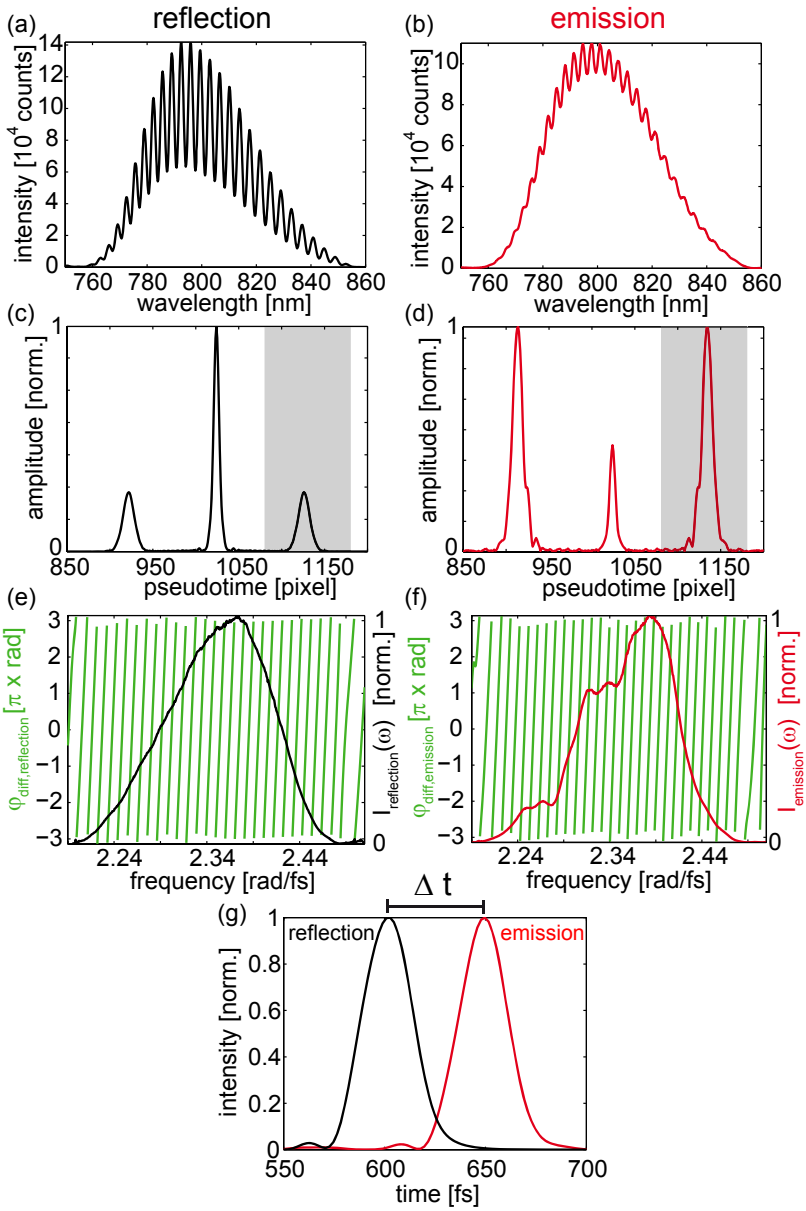

Fig. 4. Data evaluation process. The left (right) column shows data from the reflection (emission) position. (a) and (b): Spectral interferograms recorded at the respective positions of Fig. 3(b) are shown. (c) and (d): The amplitudes after the first fast Fourier transformation are depicted. Since the spectrometer detector provides 2048 pixels for the wavelength-space sampling, the non-oscillatory part is centered around pixel number 1024. The shaded area depicts the Fourier window that is used for the second (inverse) fast Fourier transformation. From this transformation the reconstructed intensity $I_i(\omega)$ and difference phase $\varphi_{\mathrm{diff},i}(\omega) = \varphi_i(\omega) - \varphi_{\mathrm{ref}}(\omega)$ can be deduced [(e) and (f)]. Employing a third fast Fourier transformation using the data of (e) and (f) yields the temporal envelopes depicted in (g). The separation time Δt is deduced from the maxima and has to be corrected for the position-dependent pulse arrival time (PD-PAT, see corresponding section) to yield the plasmon propagation time t_{prop}.

#166965 - $15.00 USD
Received 18 Apr 2012; accepted 20 May 2012; published 15 Jun 2012

4(f) this spectral-phase response function is mostly linear, since both phases $\varphi_{\mathrm{diff},i}(\omega)$ have a strong slope according to $\tau \approx 600$ fs but show little curvature. This linear slope of the response function indicates the difference in arrival time of the reflected and the emitted signal. For a detailed analysis of this time separation we employ a third fast Fourier transform using $I_i(\omega)$ and $\varphi_{\mathrm{diff},i}(\omega)$ — both zero padded at high frequencies — of the reflection and the emission signal to obtain the temporal envelopes shown in Fig. 4(g). The arrival time of the reflection pulse at ca. 600 fs (black) indicates the adjusted delay of the signal pulse with respect to the reference pulse. Because of plasmon propagation the emission (red) arrives at a time Δt later. In the case of multiple reflections of the propagating plasmon wave inside the nanowire multiple signal pulses are expected. These pulses will show up as additional (though much lower) peaks in the temporal envelopes and will not affect the data evaluation because the global maximum is evaluated only.

Due to the fact that the plasmon propagation time for the investigated micrometer-long structures is in the range of tens of femtoseconds it is important to carefully consider time offsets that may be acquired within the setup due to different optical paths. As we will see in the next section, path differences due to the different detection positions in the sample plane [cf. "Refl." and "Em." circles in Figs. 3(b) and 3(c)] translate into a position-dependent pulse arrival time (PD-PAT) and can indeed not be neglected. Consequently, the separation Δt of the maxima in Fig. 4(g) have to be corrected by the PD-PAT to yield the plasmon propagation time t_{prop}. This correction is also discussed in the next section.

4. Position-Dependent Pulse Arrival Time (PD-PAT)

Time delays due to geometrical path differences that are acquired in the microscope setup because of the different detection positions in the sample plane [cf. "Refl." and "Em." circles in Figs. 3(b) and 3(c)] translate into a position-dependent pulse arrival time (PD-PAT), which is discussed in this section.

The time delays that occur in the present setup can be accounted for by a ray-tracing model as depicted in Fig. 5. The figure shows an idealized and simplified two-dimensional scheme of the setup's part enclosed in the dashed box of Fig. 2. Signals (green and red lines) emerge from the sample plane, pass the objective, are redirected by the piezo tip-tilt mirror (black dashed for tilting position 1 and black solid for tilting position 2) and subsequently focused onto the pinhole (PH). By scanning the piezo tip-tilt mirror around its center, different sample plane positions are selected by the pinhole. The green path (1) indicates a signal emerging from the center of the sample plane. In that case, the beam path coincides with the optical axis of the objective and is reflected at the center of the piezo tip-tilt mirror. After this reflection the beam path coincides with the optical axis of lens L_1 and the signal is focused onto the pinhole in the image plane. In this setting of the piezo tip-tilt mirror (dashed black) the mirror normal and the optical axis of the objective form a 45° angle ("zero position"). On the other hand, the red path (2) indicates a signal that emerges a distance r away from the center of the sample plane. The angle α is connected to this distance via $\alpha = \arctan(r/f)$, with $f = 2$ mm being the focal length of the objective. This can be simplified to $\alpha = r/f$, since very small angels are considered ($\pm 10\ \mu$m $\widehat{=}\ \pm 0.005$ rad). With the piezo tip-tilt mirror in its "zero position" this signal (2) would not be imaged onto the pinhole. However, by tilting the piezo tip-tilt mirror about an angle of $\alpha/2$ around its center as indicated (solid black) the signal is deflected such that it passes the pinhole (see Fig. 5).

The optical path length difference between 2 and 1 (from the sample plane to the reference plane) can be obtained via trigonometry and yields (see Appendix A)

$$\bar{2} - \bar{1} = -(L_{\mathrm{obj}} n_{\mathrm{obj}} + D)\frac{\alpha^2}{2} = -\frac{A}{2}\left(\frac{r}{f}\right)^2, \tag{1}$$

#166965 - $15.00 USD Received 18 Apr 2012; accepted 20 May 2012; published 15 Jun 2012

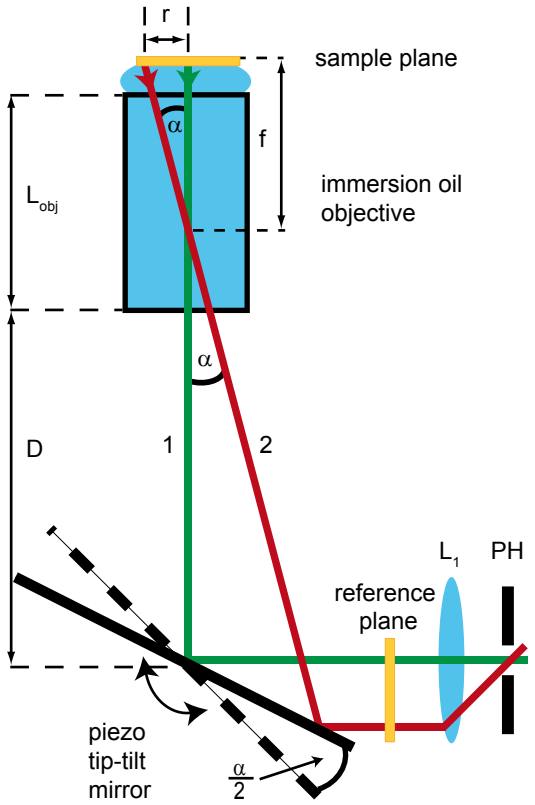

Fig. 5. Ray-tracing model for the position-dependent pulse arrival time (PD-PAT). By scanning the piezo tip-tilt mirror different sample positions are mapped onto the pinhole (PH). For the black dashed position, signal 1 (green path) emerging from the center of the sample plane is focused onto the pinhole. For the black solid position, signal 2 (red path) passes the pinhole.

with n_{obj} being the (average) refractive index and f the focal length of the objective. The distances L_{obj} and D are defined in Fig. 5. On the right hand side of this equation we introduced the PD-PAT Amplitude $A = L_{\mathrm{obj}} n_{\mathrm{obj}} + D$. The negative sign in Eq. (1) indicates that path 2 is shorter. Since the problem is rotationally symmetric, i.e., only the distance r to the sample center within the sample plane is important, signals from an outer rim in the sample plane arrive earlier at a detector behind the pinhole than signals that emerge from the center.

The field of view, i.e., the part of the sample that is imaged onto the detector, is defined by the objective. The center of the field of view is defined by the optical axis of the objective. For an excitation beam propagating parallel to this optical axis the position of the excitation focus is identical with this field of view center. In the idealized description of the PD-PAT origin above it is assumed that the center of rotation of the piezo tip-tilt mirror lies on the optical axis of the objective (green path 1). If this is not the case and the center of rotation is shifted a distance Δm with respect to the optical axis, the PD-PAT center position is displaced by the amount Δx relatively to the field of view center. In this case, the excitation/reflection position and the PD-PAT center are not the same. In our setup, a distance of $\Delta m = 1$ mm roughly corresponds to a shift of $\Delta x = 5$ μm. In order to take this alignment factor into account, we model the PD-PAT

#166965 - $15.00 USD
Received 18 Apr 2012; accepted 20 May 2012; published 15 Jun 2012

value in the sample plane as

$$T_{\mathrm{PD-PAT}}(x,y) = -\frac{A}{2c}\left(\frac{(x+\Delta x)^2+(y+\Delta y)^2}{f^2}\right), \tag{2}$$

with $(\Delta x^2+\Delta y^2)^{1/2}$ being the shift of the field of view center relative to the PD-PAT center, and the speed of light in vacuum c. In all "emission scan" images [i.e., Figs. 3(b), 3(c), and 6] the axes are labeled with respect to the PD-PAT center, i.e., the position (0,0) in these images is the PD-PAT center.

Experimental calibration of Eq. (2) determines the three parameters $A, \Delta x$, and Δy. The amplitude $A = L_{\mathrm{obj}} n_{\mathrm{obj}} + D$ can easily be measured directly at the setup [see Fig. 5, $L_{\mathrm{obj}} = 5.5$ cm, $n_{\mathrm{obj}} = 1.51$, and D=(39.7 ± 0.5) cm]. This yields a value of $A = (48.0 \pm 0.5)$ cm. In contrast, the PD-PAT center position does not necessarily coincide with the excitation/reflection position and the relative shift (Δx, and Δy) has to be determined with a different approach, which is outlined in Appendix B. With all three parameters at hand, $T_{\mathrm{PD-PAT}}(x,y)$ can be calculated for all positions within the sample plane and the PD-PAT correction can be applied to the separation time Δt from the plasmon propagation experiment (Fig. 3 and Fig. 4). This is done by calculating a correction time t_{corr} from the PD-PAT values at the reflection and emission positions $[t_{\mathrm{corr}} = T_{\mathrm{PD-PAT}}(x_{\mathrm{Refl.}}, y_{\mathrm{Refl.}}) - T_{\mathrm{PD-PAT}}(x_{\mathrm{Em.}}, y_{\mathrm{Em.}})]$. The corrected propagation time is then defined as $t_{\mathrm{prop}} = \Delta t + t_{\mathrm{corr}}$. For the calculation of the plasmon velocity $v = l/t_{\mathrm{prop}}$ the separation of the reflection and emission position is the wire length l.

5. Results and discussion

In order to demonstrate and visualize the PD-PAT, we illuminated the sample plane in a quite large area (20×20 μm^2). For this purpose, a convex lens in front of the polarizer was inserted. The focal length and position of this lens was chosen to focus the excitation beam in the back focal plane of the objective. This yields a large focal spot in the sample plane. The reflection of this large focal spot is then imaged onto the pinhole plane. The sample for this experiment is a pure glass substrate and the analyzer is set to the same orientation as the polarizer, since the direct reflection of the glass–air interface is of interest. By applying the data evaluation method (cf. Fig. 4) to every position within the sample plane (here, "reflection" = center of scanned area, "emission" = all other positions), the measured position-dependent pulse arrival time (PD-PAT) can be visualized as shown in Fig. 6(a). Note that compared to Figs. 3(b) and 3(c) the scan area now is 20×20 μm^2 and the color code represents relative arrival time rather than intensity.

As expected from the model [Eq. (2)], a rotationally symmetric dependence is visible and signals emerging further away from the center of the scanned area arrive earlier at the detector. Similar dependencies, but completely different in origin, have been found due to the radial group delay in (chromatic) lenses [25, 26]. Fitting the measured data with Eq. (2) results in an amplitude of $A = (47 \pm 1)$ cm, which agrees with the value used for calculating $T_{\mathrm{PD-PAT}}(x,y)$ $[A = (48.0 \pm 0.5)$ cm]. Furthermore, the difference of the measured and fitted time-correction data has a standard deviation of about 1 fs (data not shown), indicating that no additional parameters have to be considered in Eqs. (1) or (2).

In this demonstration experiment, the lateral positioning of the additional lens in front of the polarizer modifies the beam path towards the objective and determines the center position of the measured PD-PAT [the position of the minimum pulse delay in Fig. 6(a) is not centered at (0,0)]. Therefore, this center position has to be determined in a different fashion as discussed in Appendix B.

In Fig. 6(b) the PD-PAT calculated with Eq. (2) is shown for the same area. For the calculation the parameters $A = 48.0$ cm, $\Delta x = 0.68$ μm, and $\Delta y = 1.13$ μm were used. As a

#166965 - $15.00 USD Received 18 Apr 2012; accepted 20 May 2012; published 15 Jun 2012

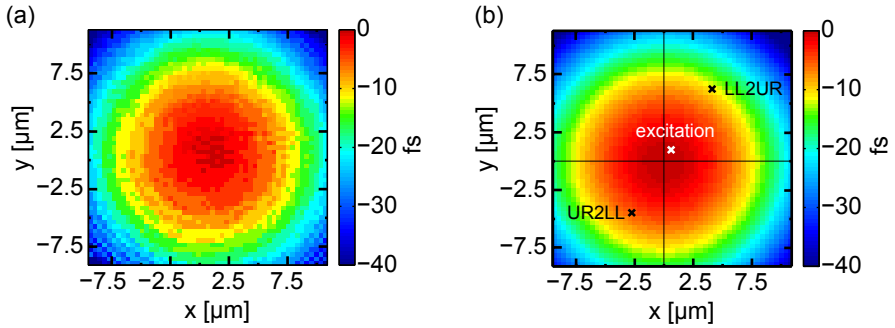

Fig. 6. Visualizations of the PD-PAT. Note that the area size is 20×20 μm^2 and the color code represents the relative arrival time. (a) The measured data that is acquired by illuminating the complete area is depicted. (b) The calculated data according to Eq. (2) is shown, where the parameters $A = 48.0$ cm, $\Delta x = 0.68$ μm, and $\Delta y = 1.13$ μm where used. The measured and calculated data agree very well. In order to connect this visualization to the plasmon propagation experiment shown in Fig. 3, the reflection and emission positions from that figure are marked here with white and black crosses, respectively.

consequence, the position of minimum pulse delay is centered at (0,0). Comparing the measured [Fig. 6(a)] and calculated [Fig. 6(b)] data reveals the very good agreement. In Fig. 6(b) the reflection and emission positions of the plasmon propagation experiment (cf. Fig. 3) are marked with white and black crosses, respectively. As can be seen, the PD-PAT center (0,0) does not coincide with the excitation/reflection position and different corrections have to be applied for both measurement directions.

By utilizing the PD-PAT correction we can, e.g., determine the group velocity of plasmons propagating along silver nanowires. We find that the velocity depends on the diameter of the nanowires and observe a drastic decrease of the velocity for nanowire diameters below 100 nm [27]. For larger diameters the velocity saturates at circa 44 % of the velocity of light in vacuum. Furthermore, we experimentally demonstrate the dependence of the plasmon group velocity on the local nanowire environment [27].

Apart from the timing information that is encoded in the first-order Taylor coefficient of the spectral-phase response function [$\varphi_{\text{response}}(\omega) = \varphi_{\text{diff,Em.}}(\omega) - \varphi_{\text{diff,Refl.}}(\omega)$], we also analyzed higher-order phase terms, i.e., the dispersion of propagating plasmon pulses. As the dispersion is very low in the case of silver nanowires, we can state only an upper limit of 50 fs^{2}rad$^{-1}\mu$m^{-1} for the experimentally determined group delay dispersion per propagation length. This value is in good agreement with data obtained from the second derivative of simulated dispersion relations [27].

The absolute errors for plasmon group velocities are calculated according to formal error propagation. Recording nine spectral interferograms at both positions ["Refl." and "Em." in Figs. 3(b) and 3(c)] for each measurement direction ("LL2UR" and "UR2LL") results in an average separation time $\langle \Delta t \rangle$. The standard error of this ensemble is usually below 1 fs and is taken as the absolute error of the mean separation time. Formal error propagation treatment of the PD-PAT formula [Eq. (2)] yields the absolute error of the PD-PAT value. Here, we assume a position inaccuracy of $\Delta x_i = \Delta y_i = 0.1$ μm. The parameters of Eq. (2) are determined (see also Appendix B) to have errors of $\Delta(\Delta x) = \Delta(\Delta y) = 0.3$ μm, and $\Delta A = 1$ cm. The total error due to different path lengths in the microscope depends on the nanowire length but is around $\Delta T_{\text{PD-PAT}} \approx 1$ fs for a length of 5 μm. Thus, the error of the final corrected propagation time t_{prop} is also on the order of 1 fs. For calculating the plasmon velocity, the inaccuracy of the

#166965 - $15.00 USD
Received 18 Apr 2012; accepted 20 May 2012; published 15 Jun 2012

measured length is assumed to be $\Delta l = 0.15\ \mu$m. The determined speeds of both measurement directions of each nanowire are averaged. The complete procedure yields final relativ errors of plasmon group velocities of ca. 3 %.

Apart from the geometrical correction (PD-PAT), no additional phase or amplitude effects of the setup have to be considered, since the relative change between reflection and emission signals is determined and such effects cancel out automatically. The reflection signal is due to a non-resonant (instantaneous) scattering process at the input end of the nanowire. The complex-valued reflection coefficient of this process is constant within the laser pulse spectrum. Therefore, the temporal position of this reflection is the correct starting time of the plasmon mode. Furthermore, possible phase offsets (i.e., zero-order Taylor coefficients) that may occur upon reflection at the nanowire input end do not matter for the determination of plasmon group velocity or dispersion of the plasmon mode upon propagation. Finally, the nanowires are indeed attached to the planar substrate surface: The reflected signal at both ends and the signal from a reflection at the center of the nanowire arrive at the same time within the experimental accuracy at the detector (data not shown).

There are two reasons for the threefold fast Fourier transform evaluation. First, reconstruction of $I_i(\omega)$ and $\varphi_{\mathrm{diff},i}(\omega)$ is necessary to calculate the spectral response function $\varphi_{\mathrm{response}}(\omega) = \varphi_{\mathrm{diff,Em.}}(\omega) - \varphi_{\mathrm{diff,Refl.}}(\omega)$ of a plasmonic element. Second, it is not possible to retrieve exact timing information from the first fast Fourier transformation, which starts in λ-space and, therefore, does not yield time-domain information. [Therefore, the abscissae in Figs. 4(c) and 4(d) are termed "pseudotime"]. It would be necessary to resample the spectral interferogram in the ω-space to directly yield time-domain information. This introduces errors due to interpolation of the highly modulated data [28], while resampling the filtered data after the second Fourier transformation does not introduce significant interpolation errors.

6. Summary and conclusions

In summary, we introduced a technique for characterization of functional plasmonic elements by combining confocal microscopy that facilitates independent excitation/detection positioning with spectral interference using ultrashort pulses. This technique enables us to characterize propagation properties of plasmons in nanostructures. Since the method provides full amplitude and phase information of the propagated signal, the spatial and spectral response functions of plasmonic functional elements such as splitters, multiplexers, switches or logic gates can be determined. With this far-field microscopy approach, the scenario of optically integrated plasmonic circuits — as depicted in Fig. 1 — is implemented.

In order to retrieve timing information of the plasmon pulses, time delays due to geometrical path differences within the setup are important. We use a model for the position-dependent pulse arrival time (PD-PAT) together with experimental calibration to achieve an accuracy of about 1 fs in time measurements. This enables us to determine the group velocity of propagating plasmons.

The setup can also be used to investigate non-linear effects on plasmon propagation as a result of ultrashort pulses exciting appropriate nanostructures. Moreover, applications are expected in the field of coherent control of optical excitations in nanostructures where the far-field laser pulse can be shaped in order to focus the plasmonic energy in space and time [29–34].

In future applications the presented technique might be combined with nonlinear spectroscopy schemes, such as transient grating or coherent 2D spectroscopy [35], to determine the third order response function with a spatial resolution down to the diffraction limit.

#166965 - $15.00 USD Received 18 Apr 2012; accepted 20 May 2012; published 15 Jun 2012

Appendix A

Here, we describe one way of deriving the optical path differences that lead to the position-dependent pulse arrival time (PD-PAT) as defined in Eq. (1). The angles in Fig. 7 are defined as follows: $\delta = \angle(\overline{AM};\overline{ME}) = \angle(\overline{EM};\overline{MP})$, $\alpha = \angle(\overline{BZ};\overline{ZA})$, $\varphi = \angle(\overline{PM};\overline{MK})$, $\beta = \angle(\overline{CM};\overline{MP})$.

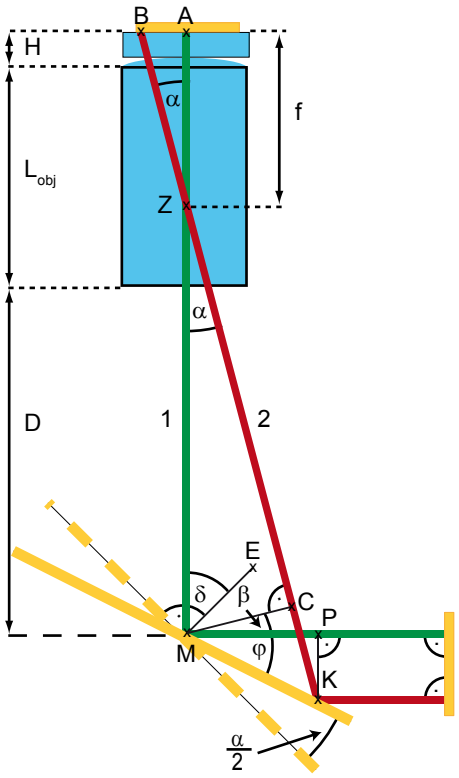

Fig. 7. Detailed schematic of Fig. 5 for trigonometric derivation of Eq. (1). $\overline{ME}$ is the normal to the untilted mirror surface (dashed orange line).

From Fig. 7 we can decompose the lengths of the optical paths 1 (green) and 2 (red) from the sample plane (AB) to the reference plane (PK):

- $\overline{1} = (H + L_{\text{obj}})n_{\text{obj}} + D + \overline{MP}$,
- $\overline{2} = \overline{BZ} + \overline{ZC} + \overline{CK}$.

The unknown length $\overline{MP}$ in path 1 can be found as follows:

- $\overline{MP} = \overline{MK}\cos\varphi$,
- $\overline{MK} = \overline{MC}/\cos(\varphi + \beta)$,
- $\overline{MC} = \{[L_{\text{obj}} - (f - H)]n_{\text{obj}} + D\}\sin\alpha$.

Thus, $\overline{MP} = \{[L_{\text{obj}} - (f - H)]n_{\text{obj}} + D\}\sin\alpha\cos\varphi/\cos(\varphi + \beta)$.

For the angles, following relations hold:

#166965 - $15.00 USD
Received 18 Apr 2012; accepted 20 May 2012; published 15 Jun 2012

- $\varphi = \frac{\pi}{2} - \frac{\alpha}{2} - \delta$,
- $(\delta + \delta - \beta) + \frac{\pi}{2} + \alpha = \pi \Leftrightarrow \beta = 2\delta - \frac{\pi}{2} + \alpha$.

Therefore, $\varphi + \beta = \frac{\alpha}{2} + \delta$, and we find
$\overline{MP} = \{[L_{\mathrm{obj}} - (f - H)]n_{\mathrm{obj}} + D\} \sin\alpha \cos(\frac{\pi}{2} - \frac{\alpha}{2} - \delta)/\cos(\frac{\alpha}{2} + \delta)$.

For the unknown lengths in path 2, we can write:

- $\overline{BZ} = (f n_{\mathrm{obj}})/\cos\alpha$,
- $\overline{ZC} = \{[L_{\mathrm{obj}} - (f - H)]n_{\mathrm{obj}} + D\} \cos\alpha$,
- $\overline{CK} = \overline{MC} \tan(\varphi + \beta)$.

If we combine all the information and mathematically simplify the optical path difference, we get

$$\overline{2} - \overline{1} = -D - (H + L_{\mathrm{obj}})n_{\mathrm{obj}} + [D + (-f + H + L_{\mathrm{obj}})n_{\mathrm{obj}}] \cos\alpha + f n_{\mathrm{obj}}/\cos\alpha. \quad (3)$$

Note that this difference is independent of the angle δ, implying that this angle does not have to be 45° and allows for a slight misalignment. In contrast, a parallel shift of the line *AM*, i.e., if the center of rotation of the piezo tip-tilt mirror does not lie on the optical axis of the objective, shifts the PD-PAT center as discussed in the main text and measured in Appendix B.

Now, we take into account that $D > L_{\mathrm{obj}} \gg f > H$ [because $D = (39.7 \pm 0.5)$ cm, $L_{\mathrm{obj}} = 5.5$ cm, $f = 2$ mm, and $H = 0.17$ mm]. In fact, this means we can assume $f = H = 0$, which reduces the optical path difference to

$$\overline{2} - \overline{1} = (L_{\mathrm{obj}} n_{\mathrm{obj}} + D)(\cos\alpha - 1). \quad (4)$$

With the assumption that we consider very small angles ($\pm 10\ \mu$m $\widehat{=}\ \pm 0.005$ rad) this formula is further simplified to Eq. (1). Both assumptions that we make, i.e., $f = H = 0$ and $\cos\alpha = 1 - \frac{\alpha^2}{2}$, create a systematic deviation of the approximation [Eq. (1)] with respect to the exact formula [Eq. (3)] that is -0.1 fs at a distance to the PD-PAT center of 5 μm, and hence is an order below the estimated PD-PAT error of $\Delta T_{\mathrm{PD-PAT}} \approx 1$ fs.

Appendix B

As explained in the main text, the propagation on each nanowire can be measured in two different directions [cf. Fig. 3(b): "LL2UR-propagation" and Fig. 3(c): "UR2LL-propagation"]. Since the coupling to the nanowire does not influence the propagation velocity, both measurement directions should yield the same result. We checked this statement by measuring, e.g., a "LL2UR-propagation", turning the sample around 180°, and performing the same experiment again (data not shown). The relative difference of the calculated velocities for both experiments, which is independent of the PD-PAT correction, was on the order of $(v_{\mathrm{LL2UR},0^\circ} - v_{\mathrm{LL2UR},180^\circ})/(v_{\mathrm{LL2UR},0^\circ}) = 2$ %, i.e., within the measurement error. For comparison, the relative difference of the velocities (calculated without applying the PD-PAT correction) for different measurement directions was mostly $(v_{\mathrm{LL2UR}} - v_{\mathrm{UR2LL}})/(v_{\mathrm{LL2UR}}) \geq 10$ %.

This consideration yields a handle for determination of the unknown parameters Δx and Δy of Eq. (2). By applying the PD-PAT correction to the determined separation times Δt_j [cf. Fig. 4(g)] of both measurement directions (j = UR2LL and j = LL2UR) for various parameter pairs Δx and Δy, these two parameters can be found under the constraint that the corrected propagation velocities for both measurement directions have to be the same. Since in fact only the

#166965 - $15.00 USD Received 18 Apr 2012; accepted 20 May 2012; published 15 Jun 2012

PD-PAT value at the excitation and emission position is fixed by this procedure, one nanowire measurement is not enough. However, by fitting the data of multiple nanowires (with different lengths and preferably different orientations) "globally" the parameters Δx and Δy can be found with sufficient accuracy. Note that no a-priori knowledge of the absolute value of the plasmon group velocity is needed for this procedure.

In our case, we measured a set of 13 nanowires in both directions. Afterwards, we used an unconstrained nonlinear optimization procedure to minimize the total squared corrected velocity differences $[\Sigma_{k=1}^{13}\left(v_{\mathrm{UR2LL},k}-v_{\mathrm{LL2UR},k}\right)^2]$ of both directions under variation of the parameters Δx and Δy. This resulted in $\Delta x = (0.68 \pm 0.3)\ \mu$m and $\Delta y = (1.13 \pm 0.3)\ \mu$m. In all "emission" figures [Figs. 3(b), 3(c), and 6] the axes are labeled with respect to the PD-PAT center, i.e., the position (0,0) is the PD-PAT center and the excitation/reflection position is at $(\Delta x, \Delta y)$. By applying the PD-PAT correction the relative difference of both measurement directions is decreased to about 2 %.

We want to note that if the PD-PAT center and the excitation/reflection position do coincide (i.e., $\Delta x = \Delta y = 0$) both measurement directions will always yield the same separation time ($\Delta t_{\mathrm{UR2LL}} = \Delta t_{\mathrm{LL2UR}}$), since the PD-PAT is rotational symmetric. By the same argument this is also true if the shift vector $\binom{\Delta x}{\Delta y}$ is normal to the nanowires's long axis. This might erroneously lead to the conclusion that no correction has to be applied for a perfect aligned system. However, it should be clear that the determined propagation velocity will always be wrong if no PD-PAT correction is applied.

Acknowledgment

This work was supported by the DFG within the Priority Program "Ultrafast Nanooptics" (SPP 1391). The authors thank A.A. Reiserer for helping to design and to build an early version of the experimental setup. This publication was funded by the German Research Foundation (DFG) and the University of Wuerzburg in the funding program Open Access Publishing.

#166965 - $15.00 USD Received 18 Apr 2012; accepted 20 May 2012; published 15 Jun 2012